Time-reversal-invariant spin-orbit-coupled bilayer Bose-Einstein condensates

Matthew Maisberger,[1] Lin-Cheng Wang,[1,2] Kuei Sun,[1] Yong Xu,[1,3] and Chuanwei Zhang[1,*]
[1]*Department of Physics, University of Texas at Dallas, Richardson, Texas 75080-3021, USA*
[2]*School of Physics, Dalian University of Technology, Dalian 116024, People's Republic of China*
[3]*Center for Quantum Information, IIIS, Tsinghua University, Beijing 100084, People's Republic of China*

(Received 3 November 2017; revised manuscript received 4 April 2018; published 29 May 2018)

Time-reversal invariance plays a crucial role for many exotic quantum phases, particularly for topologically nontrivial states, in spin-orbit coupled electronic systems. Recently realized spin-orbit coupled cold-atom systems, however, lack the time-reversal symmetry due to the inevitable presence of an effective transverse Zeeman field. We address this issue by analyzing a realistic scheme to preserve time-reversal symmetry in spin-orbit-coupled ultracold atoms, with the use of Hermite-Gaussian-laser-induced Raman transitions that preserve spin-layer time-reversal symmetry. We find that the system's quantum states form Kramers pairs, resulting in symmetry-protected gap closing of the lowest two bands at arbitrarily large Raman coupling. We also show that Bose gases in this setup exhibit interaction-induced layer-stripe and uniform phases as well as intriguing spin-layer symmetry and spin-layer correlation.

DOI: 10.1103/PhysRevA.97.053624

I. INTRODUCTION

Time-reversal invariance constitutes a fundamental symmetry in quantum physics. A half-integer spin system always possesses two-fold degenerate quantum states, or Kramers degeneracy [1], under the time-reversal symmetry. In solid-state materials, the presence of time-reversal symmetry and spin-orbit coupling, interaction between particle spin and orbital degrees of freedom, is responsible for many exotic phenomena such as quantum spin Hall effects and topological insulators [2–4], whose key physical features—a gapless edge state—is guaranteed by Kramers degeneracy. Recently, a class of exotic quantum phases has been found in ultracold atoms through the engineering of various types of spin-orbit coupling via light-matter interaction [5–10], including spin-linear-momentum coupling [11–26], which has been widely studied in experiments [27–38], and proposed spin-orbital-angular-momentum [39–44] as well as spin-tensor-momentum [45] couplings. However, in these schemes, the spin-orbit interaction is generated by a laser-induced Raman transition between atomic hyperfine states, which manifests as a constant Zeeman field along a fixed transverse direction and hence inevitably breaks the time-reversal symmetry. For further pursuit of new quantum phases with nontrivial physics due to the interplay between time-reversal symmetry and spin-orbit couplings, it is crucial to create time-reversal invariance coexisting with spin-orbit coupling in these systems.

Ongoing study has focused on the topological structure of spin-orbit-coupled degenerate Fermi gases preserving time-reversal symmetry [46]. In this paper, we provide detailed analysis on such a scheme that generates time-reversal symmetry in ultracold atoms and investigate interacting Bose-Einstein condensates (BECs) realized with it. The approach generalizes the conventional experimental scheme [27], in which two Gaussian lasers are applied to spinor gases, by replacing one laser beam with a first-order Hermite-Gaussian (HG) beam [47] [see Fig. 1(a)]. The HG beam induces spin-orbit coupling in each layer and preserves the bilayer system under time-reversal operation,

$$\Theta = i\sigma_y\tau_x K, \tag{1}$$

where $\boldsymbol{\sigma}$ and $\boldsymbol{\tau}$ are Pauli matrices in spin and layer space, respectively, and K is the conjugate operator. Note that Θ, though involving the layer degrees of freedom, exhibits the same physical properties as the regular time-reversal operator by being anti-unitary and $\Theta^2 = -1$. While this symmetry is crucial for nontrivial topological states in Fermi-gas [46] and solid-state [48] systems, here we focus on interacting Bose gases in this setup. We find rich phase diagrams as well as interesting correlations that are not present in regular spin-orbit-coupled BECs without this time-reversal symmetry. Our main results are summarized below:

(i) The system's single-particle energy bands pair as time-reversal partners and are also subject to a spin-layer symmetry $\sigma_z\tau_x$. The Kramers degeneracy prevents the gap opening between the paired bands at zero momentum, resulting in double finite-momentum band minima that always exist, i.e., the zero-momentum state can never be the single-particle ground state even at a large Raman coupling, unless the two layers completely decouple.

(ii) The interacting phase diagram of a ground-state Bose gas exhibits layer-stripe, plane-wave, and zero-momentum phases. The layer-stripe phase (and its Kramers partner), occurring at weak Raman coupling, exhibits spatially modulating layer polarization but no total density modulation due to the time-reversal symmetry. At large interaction and large Raman coupling, the many-body effects drive the BEC to a zero-momentum ground state (or its Kramers partner), even if the zero momentum is not the single-particle band minimum.

*Corresponding author: chuanwei.zhang@utdallas.edu

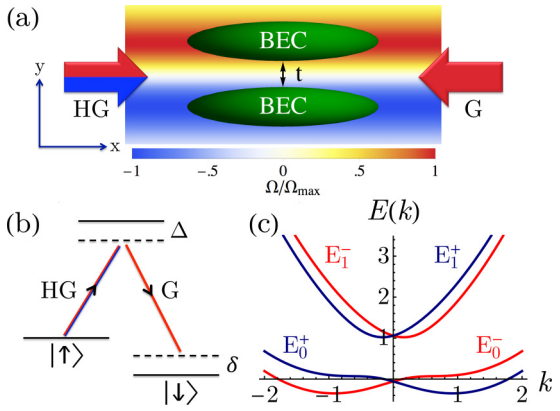

FIG. 1. (a) Scheme for generating spin-orbit-coupled BECs preserving time-reversal symmetry. A pair of counter-propagating Gaussian (G) and Hermite-Gaussian (HG) beams induces a Raman transition that has opposite amplitudes between upper ($y > 0$, red) and lower ($y < 0$, blue) regions. An additional far-detuned HG laser beam can be used to create a bilayer structure with interlayer tunneling t. (b) The Raman transition process between the atomic hyperfine levels. (c) The single-particle energy dispersion of the system at $\Omega = 1$ and $t = 0.5$. The band crossing at $k = 0$ is time-reversal symmetry protected. Each band also satisfies a spin-layer symmetry $\langle \sigma_z \tau_x \rangle = \pm 1$ (light red and dark blue, respectively).

(iii) The Bose gas exhibits a global spin-layer correlation $\langle \sigma_x \tau_z \rangle \neq 0$, while either the spin or the layer component vanishes, $\langle \sigma_x \rangle = \langle \tau_z \rangle = 0$. It is crucial for experiments to measure spin and layer properties simultaneously rather separately.

We present the details of (i) in Sec. II and those of (ii) and (iii) in Sec. III, followed by experimental considerations in Sec. IV and a conclusion in Sec. V.

II. MODEL AND HAMILTONIAN

We start with ultracold atoms with two hyperfine spin states $(\psi_\uparrow \quad \psi_\downarrow)^T$, subject to a pair of counter-propagating lasers $\Omega_L^{\pm}$ along the x direction, with transverse electromagnetic modes of a general Hermite form. The laser amplitudes are

$$\Omega_{m,n}^{\pm} = A H_m\left(\frac{\sqrt{2}y}{w}\right) H_n\left(\frac{\sqrt{2}z}{w}\right) e^{-\frac{y^2+z^2}{w^2} \pm i k_R x},$$

where A represents the overall beam strength, H_n is the nth Hermite polynomials, w is the beam waist, and k_R is the wave vector. The two beams impart spin-dependent linear momentum into the atoms and also induce Raman transition $\Omega_R(\boldsymbol{r}) = \Omega^{+*}\Omega^{-}/\Delta$ between the spin states, as shown in Fig. 1(b) (Δ is a uniform detuning). If both beams are of the lowest mode $\Omega_{0,0}^{\pm}$ (two Gaussian beams), we have the regular setup for generating the spin-linear-momentum coupling. Here, we focus on a practical generalization to $\Omega_{1,0}^{+}$ and $\Omega_{0,0}^{-}$, i.e., left-propagating Gaussian and right-propagating HG beams, as shown in Fig. 1(a). The Raman transition amplitude $\Omega_R(\boldsymbol{r})$ now has an odd spatial parity along the y direction with maximum strength at $y = \pm w/\sqrt{2}$. Along the y direction, a bilayer trapping potential can be realized using a repulsive potential at the center of a tight harmonic trap or a single far-detuning HG laser beam of the (1,0) mode. Such additional far-detuning trapping lasers avoid the heating from the trapping and ensure the independent tunability of the interlayer tunneling. Performing a unitary transformation $\psi_{\uparrow,\downarrow} \to \psi_{\uparrow,\downarrow} e^{\mp i k_R x}$ and integrating out the y and z degrees of freedom, we obtain the effective Hamiltonian for upper and lower layers, respectively, as $\frac{1}{2}(p_x^2 - 2p_x\sigma_z \pm \Omega\sigma_x)$, where $p_x\sigma_z$ is the spin-orbit coupling and Ω is the effective Raman coupling. Here we take k_R and $\hbar^2 k_R^2/2m$ as momentum and energy units, respectively (m is the atomic mass). The only difference between the two layers is the opposite sign of Raman coupling due to the HG beam. If the two layers have a slight overlap, the dominant interlayer coupling is particle tunneling between the two layers. We can treat the two layers as another two-level degrees of freedom and write down the whole Hamiltonian in spin-layer basis $(\psi_{1\uparrow} \quad \psi_{1\downarrow} \quad \psi_{2\uparrow} \quad \psi_{2\downarrow})^T$ as

$$H = \tfrac{1}{2}\left(p_x^2 - 2p_x\sigma_z + \Omega\sigma_x\tau_z - t\tau_x\right), \tag{2}$$

where t is the tunneling strength. Note that the system in general can have a detuning term $\delta\sigma_z$ [as shown in Fig. 1(b)], which has to be tuned to zero for the time-reversal symmetry we are interested in.

The Hamiltonian exhibits a spin-layer time-reversal symmetry,

$$\Theta H(p_x)\Theta^{-1} = H(-p_x), \tag{3}$$

under which the lower two energy bands,

$$E_0^{\pm}(k) = \tfrac{1}{2}(k^2 - \sqrt{(2k \pm t)^2 + \Omega^2}), \tag{4}$$

become time-reversal partners, i.e., $E_0^+(k)$ and $E_0^-(-k)$ form degenerate Kramers pairs, as shown in Fig. 1(c). The fact $E_0^+(0) = E_0^-(0)$ leads to a symmetry-protected band crossing (or gap closing) at $k = 0$. Similarly, the upper two bands $E_1^{\pm}(k) = \frac{1}{2}[k^2 + \sqrt{(2k \pm t)^2 + \Omega^2}]$ are also time-reversal partners crossing at $k = 0$. At $\Omega = 0$, the energy band exhibits double minima at $\pm k_{\min} = \pm 1$. As Ω increases, $k_{\min}$ shifts toward the zero momentum and approaches $k_{\min} = \frac{t}{\Omega - 2} + O(\Omega^{-3})$ in the large Ω limit ($\Omega \gg 2$). As a result, the single-particle ground states are doubly degenerate and always possess finite momentum $\pm k_{\min} \neq 0$—the crossing point $k = 0$ can never be the ground state—with the presence of interlayer coupling $t \neq 0$. If the layers are completely decoupled, or $t = 0$, the lower bands $E_0^{\pm}(k)$ become identical, and the ground states undergo a transition from finite to zero momentum at $\Omega_c = 2$, the same critical value as in the conventional spin-orbit-coupled system.

In addition to the time-reversal symmetry, the Hamiltonian also exhibits a spin-layer symmetry,

$$[H, \sigma_z\tau_x] = 0. \tag{5}$$

We find that the paired bands $E_0^{\mp}$ (or $E_1^{\mp}$) are subject to $\langle \sigma_z\tau_x \rangle = \pm 1$ [light red and dark blue colors in Fig. 1(c), respectively]. By measuring this symmetry, one could distinguish a state from its Kramers partner.

III. INTERACTING BOSE GASES

We consider an interacting Bose gas in this time-reversal-invariant setup and study its ground-state properties as a function of system parameters. We use two complementary

methods, variational analysis and Gross-Pitaevskii equation (GPE) numerics, to find the BEC ground-state wave function. Both methods show fair agreement on the results presented in this section.

We adopt a variational wave function as a general superposition of a Kramers pair as

$$\Psi = \sqrt{\rho}\left[|C_1|\begin{pmatrix}\cos\theta\cos\gamma_1 e^{i\delta_1}\\ \cos\theta\sin\gamma_1 e^{i\delta_2}\\ \sin\theta\cos\gamma_2 e^{i\delta_3}\\ \sin\theta\sin\gamma_2\end{pmatrix}e^{ik_1x} + |C_2|\begin{pmatrix}\sin\theta\sin\gamma_2\\ -\sin\theta\cos\gamma_2 e^{-i\delta_3}\\ \cos\theta\sin\gamma_1 e^{-i\delta_2}\\ -\cos\theta\cos\gamma_1 e^{-i\delta_1}\end{pmatrix}e^{-ik_1x}\right], \quad (6)$$

with particle number density ρ and normalization condition $|C_1|^2 + |C_2|^2 = 1$. The ansatz is generalized from the conventional spin-orbit-coupled system but respects the time-reversal associated degeneracy. By setting $\theta = \pi/4$ and $\gamma_1 = \gamma_2$, the top-layer components of Ψ reproduce the previous results without time-reversal symmetry in Ref. [18]. Note that the ground-state wave function of this type is also confirmed by our GPE calculations, which are not bound to any constraint.

The BEC's energy density is expressed as

$$\varepsilon = \int dx\left[\Psi^\dagger H\Psi + \frac{g}{2}|\Psi|^4 + g_{\uparrow\downarrow}\sum_{j=1,2}|\psi_{j\uparrow}|^2|\psi_{j\downarrow}|^2\right], \quad (7)$$

where g and $g_{\uparrow\downarrow}$ are interatomic interactions between same and opposite spin species, respectively. Inserting Eq. (6) into Eq. (7), we obtain the energy density as a functional of eight independent variables k_1, $|C_1|$, θ, $\gamma_{1,2}$, and $\delta_{1,2,3}$ (see the Appendix). Minimizing the functional with respect to the variables, we obtain the ground-state wave function. We remark that $\Theta\Psi$, the time-reversal state of Ψ, is always orthogonal to Ψ and gives the same energy functional ε. This means that the ground states are always doubly degenerate and are time-reversal partners of each other. The variational ansatz also allows us to compute the associated physical properties as

$$\begin{aligned}
\langle\sigma_z\rangle &= (\cos^2\theta\cos 2\gamma_1 + \sin^2\theta\cos 2\gamma_2)(|C_1|^2 - |C_2|^2),\\
\langle\sigma_x\rangle &= [\sin 2\gamma_1\cos^2\theta\cos\delta_{12} + \sin 2\gamma_2\sin^2\theta\cos\delta_3]\\
&\quad\times(|C_1|^2 - |C_2|^2),\\
\langle\sigma_x\tau_z\rangle &= \cos^2\theta\sin 2\gamma_1\cos\delta_{12} - \sin^2\theta\sin 2\gamma_2\cos\delta_3,\\
\langle\sigma_z\tau_x\rangle &= \sin 2\theta[\cos\gamma_1\cos\gamma_2\cos\delta_{13} - \sin\gamma_1\sin\gamma_2\cos\delta_2]\\
&\quad\times(|C_1|^2 - |C_2|^2), \quad (8)
\end{aligned}$$

where $\delta_{ij} \equiv \delta_i - \delta_j$.

The interacting ground state exhibits three phases: (I) layer-stripe phase having $k_1 \neq 0$, $|C_1| = |C_2| = \frac{1}{\sqrt{2}}$, and $\langle\sigma_z\rangle = \langle\sigma_x\rangle = \langle\sigma_z\tau_x\rangle = 0$ (resulting in spatially modulated layer polarization as we will show in Sec. III); (II) plane-wave phase having $k_1 \neq 0, |C_1C_2| = 0, |\langle\sigma_z\rangle| > 0$, and $|\langle\sigma_z\tau_x\rangle| = 1$; (III) zero-momentum phase having $k_1 = |\langle\sigma_z\rangle| = 0$. Below we present the phase diagram and discuss the physics in details.

We first look at typical phase transitions for moderately interacting BEC $(g, g_{\uparrow\downarrow}) = (1, 0.9)$ as the Raman strength Ω varies. Figure 2(a) shows the momentum k_1 as a monotonically decreasing function of Ω for either coupled ($t = 0.5$, solid green curve) or decoupled ($t = 0$, dashed purple curve) layers. At small Ω, the system is in the layer-stripe phase (I). As Ω increases, the k_1 curves exhibit discontinuities, at which the system undergoes a first-order phase transition to the plane-wave phase (II). With further increase in Ω, the k_1 curve of decoupled layers drops to zero at a critical value, representing a second-order transition to the zero-momentum phase (III), while that of coupled layers smoothly decreases but does not drop to zero, i.e., no transition to phase (III). The disappearance of phase (III) due to the interlayer coupling agrees with the single-particle physics we discuss above.

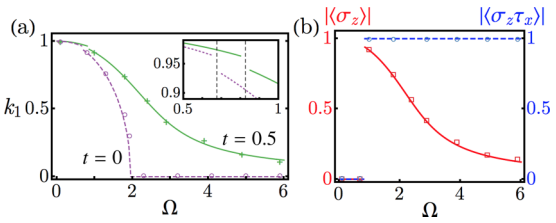

FIG. 2. (a) Momentum k_1 vs Raman strength Ω for cases of decoupled layers $t = 0$ (purple dashed) and coupled layers $t = 0.5$ (green solid). The discontinuity in both curves (enlarged in the inset) indicates the transition between layer-stripe and plane-wave phases. In the $t = 0$ case, the plane-wave phase can make a transition to the zero-momentum phase (k_1 dropping to zero), which does not occur at $t = 0.5$. (b) Spin polarization $|\langle\sigma_z\rangle|$ (red solid) and spin-layer symmetry $|\langle\sigma_z\tau_x\rangle|$ (blue dashed) vs Ω at $t = 0.5$. Note that both curves are zero and hence overlap each other in the layer-stripe phase region at small Ω. In both (a) and (b), the interaction is set to $(g, g_{\uparrow\downarrow}) = (1, 0.9)$, and curves (symbols) represent the variational (numerical GPE) results.

Figure 2(b) shows spin polarization $|\langle\sigma_z\rangle|$ and spin-layer symmetry $|\langle\sigma_z\tau_x\rangle|$ as a function of Ω for the $t = 0.5$ case. We see that the layer-stripe phase (I) is spin unpolarized $|\langle\sigma_z\rangle| = 0$, while the plane-wave phase (II) is spin polarized, so the big jump in spin polarization provides a good measurable signature for the (I)–(II) transition. The spin-layer symmetry $|\langle\sigma_z\tau_x\rangle| = 0$ in the layer-stripe phase indicates an interaction-induced symmetry breaking that equally mixes two states of opposite symmetry. In both Figs. 2(a) and 2(b), the results of variational (curves) and GPE (symbols) calculations agree with each other.

We turn to explore the interacting ground-state phases in a wide parameter region. Figure 3(a) shows the ground-state phase diagram in the g-Ω plane for $t = 0.5$ and $g_{\uparrow\downarrow} = 0.9g$. We see that the (I)–(II) phase transition is allowed in $0 < g < 40$, in which the layer-stripe phase region increases with g. In $g > 40$, the plane-wave phase (II) disappears, and the system make transitions from layer-stripe (I) to zero-momentum (III) phases. Since the zero-momentum state is never energetically favored by the single-particle Hamiltonian with finite t, the zero-momentum phase here is fully attributed to the interaction effect. In fact, the system staying at the zero-momentum state costs higher single-particle energy but saves more ferromagnetic interaction energy $\propto (g - g_{\uparrow\downarrow})\rho$. Experimentally, this region can be achieved by increasing the atomic two-body scattering length through the Feshbach resonance [49] as well as the atomic density.

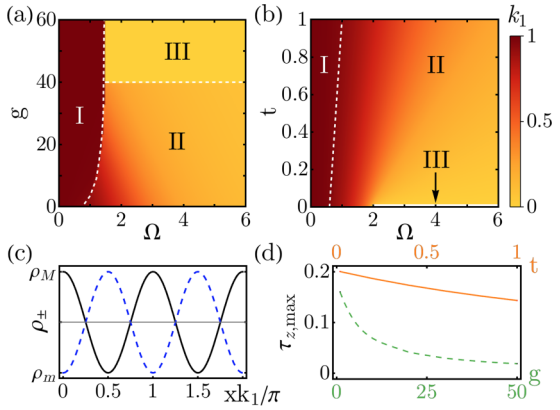

FIG. 3. (a) Phase diagram in the g-Ω plane for $t = 0.5$. In $g < 40$ (> 40), the system undergoes a transition from the layer-stripe phase (I) to the plane-wave phase (II) [zero-momentum phase (III)]. (b) Phase diagram in the t-Ω plane for $g = 1$. The zero-momentum phase only occurs in the case of decoupled layers $t = 0$ at $\Omega > 2$. The color in both (a) and (b) represents momentum k_1, as scaled in the bar graph. (c) Top (black solid) and bottom (blue dashed) layer density profiles $\rho_\pm(x)$ of a layer-stripe phase at $\Omega = t = 0.5$ in (b), exhibiting out-of-phase modulations between maximum ρ_M and minimum ρ_m, or spatial modulations in $\langle\tau_z\rangle$. (d) Modulation amplitude $\tau_{z,\max}$ [$\equiv (\rho_M - \rho_m)/2$] vs t (orange solid, top axis) and g (green dashed, bottom axis). The interspin interaction is set to be $g_{\uparrow\downarrow} = 0.9g$ for all panels.

Figure 3(a) shows similarities and essential differences compared with the phase diagram of conventional spin-orbit-coupled systems (e.g., as in Ref. [18]). While both cases exhibit the three phases and the transition from stripe (I) to plane-wave (II) phases as Ω increases, our system does not have the transition from plane-wave (II) to zero-momentum (III) phases as Ω further increases (at any nonzero t). Since the zero-momentum ground state (III) is never favored on the single-particle band of our system, its appearance in the interacting phase diagram is purely driven by (strong) interaction. Note that in the conventional system, the transition between plane-wave (II) to zero-momentum (III) states already exists in the single-particle case, while the interaction shifts the (II)–(III) phase boundary but does not make any qualitative change.

Additionally, we present in Fig. 3(b) the phase diagram in the t-Ω plane for fixed $(g, g_{\uparrow\downarrow}) = (1, 0.9)$. We see that interlayer tunneling linearly increases the layer-stripe phase region with respect to Ω. In the plane-wave phase (II), the system momentum increases with t at given Ω. The zero-momentum phase (III) appears only at $t = 0$, in which the system returns to the conventional spin-orbit-coupled BEC and hence exhibits the (II)–(III) transition as shown in Fig. 2(a).

We further look into the detailed structure of the layer-stripe phase. Figure 3(c) shows the top and bottom layer density profiles, respectively, of a layer-stripe state Ψ_s at $\Omega = t = 0.5$ and $(g, g_{\uparrow\downarrow}) = (1, 0.9)$. The two profiles show out-of-phase spatial modulations, or in other words, the system exhibits no total density modulation but a layer-polarization stripe pattern $\tau_z(x) = \Psi_s^*(x)\tau_z\Psi_s(x)$ with wavelength $\lambda_s = \pi/k_1$. The zero total density modulation is a direct consequence of time-reversal symmetry, which makes the plane-wave states of

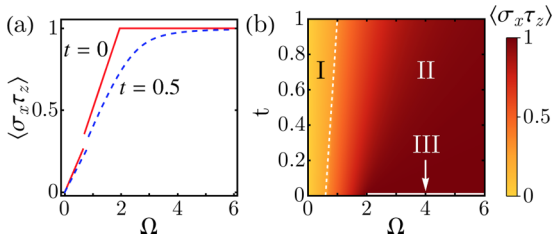

FIG. 4. (a) Spin-layer correlation $\langle\sigma_x\tau_z\rangle$ vs Raman strength Ω in the case of decoupled layers $t = 0$ (red solid) and coupled layers $t = 0.5$ (blue dashed). (b) Phase diagram in the t-Ω plane with color scale representing $\langle\sigma_x\tau_z\rangle$. In both (a) and (b), the interaction is set to $(g, g_{\uparrow\downarrow}) = (1, 0.9)$.

k and $-k$ in Eq. (6) orthogonal to each other at any spatial point. Note that in the conventional system of Ref. [18] or a bilayer system with same-sign Raman coupling on both layers, the stripe phase exhibits total density modulations. Moreover, our layer-stripe phase is doubly degenerate. The other degenerate state is the Kramers partner $\Theta\Psi_s$, which has a time-reversed layer-polarization modulation $-\tau_z(x)$. Figure 3(d) shows the oscillation amplitude of $\tau_z(x)$, denoted by $\tau_{z,\max}$, vs tunneling strength t and interaction strength g. We see that this quantity decreases as either t or g increases.

Finally, we reveal an intrinsic spin-layer correlation $\langle\sigma_x\tau_z\rangle$ of the bilayer BEC. We notice that all three phases of the system are unpolarized in the x-spin direction $\langle\sigma_x\rangle = 0$ and density balanced between the two layers $\langle\tau_z\rangle = 0$. However, the product observable of both quantities $\langle\sigma_x\tau_z\rangle$ does exhibit a nonzero expectation value. Note that when two layers have the same Ω, $\langle\sigma_x\tau_z\rangle$ is always zero. In Fig. 4(a) we plot $\langle\sigma_x\tau_z\rangle$ vs Ω for $t = 0$ and 0.5 at $(g, g_{\uparrow\downarrow}) = (1, 0.9)$. As Ω increases there is a gradual increase in the spin-layer correlation, along with a discontinuity in the curves that represents a (I)–(II) phase transition for both coupled and decoupled layers. When our system is in the zero-momentum phase we see that $\langle\sigma_x\tau_z\rangle = 1$, which is only the case for $t = 0$ at such low interaction strengths. Figure 4(b) shows the ground-state phase diagram in the t-Ω plane with color denoting $\langle\sigma_x\tau_z\rangle$. The layer-stripe phase has relatively small correlations compared with the plane-wave phase. Such a spin-layer correlation is particularly useful for characterizing the phase diagram in experiments.

IV. EXPERIMENTAL CONSIDERATION

The experimental conditions for our time-reversal invariant system are similar to but slightly modified from the current setups. We consider a ^{87}Rb bilayer BEC created in a quasi-one-dimensional harmonic trap in the x direction and a double-well-shaped potential in the y direction. The wavelength of the HG Raman laser is 788 nm, which corresponds to the recoil energy $E_R = h \times 3697$ Hz. If one tunes the bilayer separation to be 0.4 μm and the double-well barrier to be $2E_R$, the effective tunneling is $t = 0.2E_R$, with which important physics of our model can be explored. Higher tunneling is achievable by decreasing the separation or the barrier.

The layer-stripe phase can be detected by the standard time-of-fight (TOF) image, showing the co-occupation of both momentum minima. The out-of-phase stripe pattern may be

probed with the Bragg diffraction, which has successfully revealed the density stripe structure of ultracold atomic gases [50]. Moreover, we suggest the use of spin-layer correlation $\langle\sigma_x\tau_z\rangle$ to experimentally determine the phase diagram and phase transitions. In experiment, such correlation must be determined by performing both spin-resolved and layer-resolved measurements. Simply measuring spin or layer components leads to trivial results.

V. CONCLUSION

We have investigated a realistic setup for preserving time-reversal symmetry in spin-orbit-coupled quantum gases. Our approach has generalized the conventional setup to the use of HG-beam-induced Raman transitions, which create spin-orbit coupling with opposite Zeeman fields for a bilayer quantum gas. As a result, the system preserves time-reversal symmetry as well as spin-layer symmetry. We have found that unlike the conventional system, the time-reversal symmetry in our system leads to paired single-particle bands due to Kramers degeneracy, which prevents the gap opening between the lowest two bands and also the transition from double-minimum to single-minimum band structures as the Raman coupling increases.

We have investigated interacting Bose-Einstein condensates in this time-reversal invariant bilayer setup. Our results show that the ground-state phase diagram exhibits interaction-induced layer-stripe and zero-momentum phases that cannot be characterized by single-particle physics, as well as a plane-wave phase analogous to the single-particle state. The layer-stripe phase exhibits spatially modulated layer polarization. The zero-momentum phase results from a strong ferromagnetic interaction effect that overwhelms the single-particle energetic favor. We have identified the parameter region for each phase and revealed salient experimental signatures for the phase transitions. Our work allows extensive study of the time-reversal-invariant physics in various spin-orbit-coupled cold-atom systems, including dynamical features of the BEC and ground-state and excitation properties of degenerate Fermi gases as well as high-spin atomic superfluids. Another interesting direction is to investigate the time-reversal-invariant quantum gases with higher dimensional spin-orbit coupling, in which rich Kramers degeneracies may exist [51,52].

ACKNOWLEDGMENTS

This work is supported by AFOSR (FA9550-16-1-0387), NSF (PHY-1505496), and ARO (W911NF-17-1-0128). L.W. acknowledges support from National Natural Science Foundation of China (NSFC) under Grant No. 11475037 and Fundamental Research Funds for the Central Universities under Grant No. DUT15LK26.

M.M. and L.-C.W. contributed equally to this work.

APPENDIX: VARIATIONAL ENERGY FUNCTIONAL

Using the variational wave function of Eq. (6), we find an analytical expression for the energy functional of Eq. (7). For the single-particle energy, we have

$$\begin{aligned}\varepsilon_0 = {} & \frac{k_0^2}{2} + \frac{k_1^2}{2} - k_1 k_0(\cos^2\theta\cos 2\gamma_1 + \sin^2\theta\cos 2\gamma_2) \\ & + \frac{\Omega}{2}(\cos^2\theta\sin 2\gamma_1\cos\delta_{21} - \sin^2\theta\sin 2\gamma_2\cos\delta_3) \\ & - \frac{t}{2}\sin 2\theta(\cos\gamma_1\cos\gamma_2\cos\delta_{13} + \sin\gamma_1\sin\gamma_2\cos\delta_2).\end{aligned} \tag{A1}$$

For the interaction energy, we have the intraspin interaction,

$$\begin{aligned}\varepsilon_g = {} & \frac{ng}{2}\Big[(1-2\beta)\Big(\cos^4\theta\cos^4\gamma_1 + \cos^4\theta\sin^4\gamma_1 \\ & + \frac{3\sin^4\theta}{4} + \frac{\sin^4\theta\cos 4\gamma_2}{4}\Big) \\ & + 2\beta\sin^2 2\theta(\cos^2\gamma_2\sin^2\gamma_1 + \cos^2\gamma_1\sin^2\gamma_2)\Big],\end{aligned} \tag{A2}$$

where $\beta = |C_1|^2|C_2|^2$, and the interspin interaction,

$$\begin{aligned}\varepsilon_f = {} & \frac{ng_{\uparrow\downarrow}}{4}(1-2\beta)(\cos^4\theta\sin^2 2\gamma_1 + \sin^4\theta\sin^2 2\gamma_2) \\ & + ng_{\uparrow\downarrow}\beta\cos^2\theta\sin^2\theta[2\cos^2\gamma_1\cos^2\gamma_2 + 2\sin^2\gamma_1\sin^2\gamma_2 \\ & - \sin 2\gamma_1\sin 2\gamma_2\cos(\delta_1 - \delta_2 - \delta_3)].\end{aligned} \tag{A3}$$

Combining these we get the full energy functional $\varepsilon = \varepsilon_0 + \varepsilon_g + \varepsilon_f$.

[1] H. A. Kramers, Théorie générale de la rotation paramagnétique dans les cristaux, Proc. Amsterdam Acad. **33**, 959 (1930).

[2] D. Xiao, M.-C. Chang, and Q. Niu, Berry phase effects on electronic properties, Rev. Mod. Phys. **82**, 1959 (2010).

[3] X.-L. Qi and S.-C. Zhang, Topological insulators and superconductors, Rev. Mod. Phys. **83**, 1057 (2011).

[4] C.-K. Chiu, J. C. Y. Teo, A. P. Schnyder, and S. Ryu, Classification of topological quantum matter with symmetries, Rev. Mod. Phys. **88**, 035005 (2016).

[5] J. Higbie and D. M. Stamper-Kurn, Periodically Dressed Bose-Einstein Condensate: A Superfluid with an Anisotropic and Variable Critical Velocity, Phys. Rev. Lett. **88**, 090401 (2002).

[6] I. B. Spielman, Raman processes and effective gauge potentials, Phys. Rev. A **79**, 063613 (2009).

[7] J. Dalibard, F. Gerbier, G. Juzeliūnas, and P. Öhberg, Colloquium: Artificial gauge potentials for neutral atoms, Rev. Mod. Phys. **83**, 1523 (2011).

[8] V. Galitski and I. B. Spielman, Spin-orbit coupling in quantum gases, Nature **494**, 49 (2013).

[9] N. Goldman, G. Juzeliūnas, P. Öhberg, and I. B. Spielman, Light-induced gauge fields for ultracold atoms, Rep. Prog. Phys. **77**, 126401 (2014).

[10] H. Zhai, Degenerate quantum gases with spin-orbit coupling: A review, Rep. Prog. Phys. **78**, 026001 (2015).

[11] T. D. Stanescu, B. Anderson, and V. Galitski, Spin-orbit coupled Bose-Einstein condensates, Phys. Rev. A **78**, 023616 (2008).

[12] C. Wang, C. Gao, C.-M. Jian, and H. Zhai, Spin-Orbit Coupled Spinor Bose-Einstein Condensates, Phys. Rev. Lett. **105**, 160403 (2010).
[13] C. Wu, I. Mondragon-Shem, and X.-F. Zhou, Unconventional Bose-Einstein Condensations from Spin-Orbit Coupling, Chin. Phys. Lett. **28**, 097102 (2011).
[14] T.-L. Ho and S. Zhang, Bose-Einstein Condensates with Spin-Orbit Interaction, Phys. Rev. Lett. **107**, 150403 (2011).
[15] Y. Zhang, L. Mao, and C. Zhang, Mean-Field Dynamics of Spin-Orbit Coupled Bose-Einstein Condensates, Phys. Rev. Lett. **108**, 035302 (2012).
[16] H. Hu, B. Ramachandhran, H. Pu, and X.-J. Liu, Spin-Orbit Coupled Weakly Interacting Bose-Einstein Condensates in Harmonic Traps, Phys. Rev. Lett. **108**, 010402 (2012).
[17] T. Ozawa and G. Baym, Stability of Ultracold Atomic Bose Condensates with Rashba Spin-Orbit Coupling against Quantum and Thermal Fluctuations, Phys. Rev. Lett. **109**, 025301 (2012).
[18] Y. Li, L. P. Pitaevskii, and S. Stringari, Quantum Tricriticality and Phase Transitions in Spin-Orbit Coupled Bose-Einstein Condensates, Phys. Rev. Lett. **108**, 225301 (2012).
[19] M. Gong, S. Tewari, and C. Zhang, BCS-BEC Crossover and Topological Phase Transition in 3D Spin-Orbit Coupled Degenerate Fermi Gases, Phys. Rev. Lett. **107**, 195303 (2011).
[20] H. Hu, L. Jiang, X.-J. Liu, and H. Pu, Probing Anisotropic Superfluidity in Atomic Fermi Gases with Rashba Spin-Orbit Coupling, Phys. Rev. Lett. **107**, 195304 (2011).
[21] Z.-Q. Yu and H. Zhai, Spin-Orbit Coupled Fermi Gases across a Feshbach Resonance, Phys. Rev. Lett. **107**, 195305 (2011).
[22] C. Qu, Z. Zheng, M. Gong, Y. Xu, Li Mao, X. Zou, G. Guo, and C. Zhang, Topological superfluids with finite-momentum pairing and Majorana fermions, Nat. Commun. **4**, 2710 (2013).
[23] W. Zhang and W. Yi, Topological Fulde-Ferrell-Larkin-Ovchinnikov states in spin-orbit-coupled Fermi gases, Nat. Commun. **4**, 2711 (2013).
[24] K. Sun, C. Qu, Y. Xu, Y. Zhang, and C. Zhang, Interacting spin-orbit-coupled spin-1 Bose-Einstein condensates, Phys. Rev. A **93**, 023615 (2016).
[25] G. Martone, F. Pepe, P. Facchi, S. Pascazio, and S. Stringari, Tricriticalities and Quantum Phases in Spin-Orbit-Coupled Spin-1 Bose Gases, Phys. Rev. Lett. **117**, 125301 (2016).
[26] Z.-Q. Yu, Phase transitions and elementary excitations in spin-1 Bose gases with Raman-induced spin-orbit coupling, Phys. Rev. A **93**, 033648 (2016).
[27] Y.-J. Lin, K. Jiménez-García, and I. B. Spielman, Spin-orbit-coupled Bose-Einstein condensates, Nature (London) **471**, 83 (2011).
[28] J.-Y. Zhang, S.-C. Ji, Z. Chen, L. Zhang, Z.-D. Du, B. Yan, G.-S. Pan, B. Zhao, Y.-J. Deng, H. Zhai, S. Chen, and J.-W. Pan, Collective Dipole Oscillations of a Spin-Orbit Coupled Bose-Einstein Condensate, Phys. Rev. Lett. **109**, 115301 (2012).
[29] C. Qu, C. Hamner, M. Gong, C. Zhang, and P. Engels, Observation of Zitterbewegung in a spin-orbit-coupled Bose-Einstein condensate, Phys. Rev. A **88**, 021604(R) (2013).
[30] A. J. Olson, S.-J. Wang, R. J. Niffenegger, C.-H. Li, C. H. Greene, and Y. P. Chen, Tunable Landau-Zener transitions in a spin-orbit-coupled Bose-Einstein condensate, Phys. Rev. A **90**, 013616 (2014).
[31] C. Hamner, C. Qu, Y. Zhang, J. Chang, M. Gong, C. Zhang, and P. Engels, Dicke-type phase transition in a spin-orbit-coupled Bose-Einstein condensate, Nat. Commun. **5**, 4023 (2014).
[32] P. Wang, Z.-Q. Yu, Z. Fu, J. Miao, L. Huang, S. Chai, H. Zhai, and J. Zhang, Spin-Orbit Coupled Degenerate Fermi Gases, Phys. Rev. Lett. **109**, 095301 (2012).
[33] L. W. Cheuk, A. T. Sommer, Z. Hadzibabic, T. Yefsah, W. S. Bakr, and M. W. Zwierlein, Spin-Injection Spectroscopy of a Spin-Orbit Coupled Fermi Gas, Phys. Rev. Lett. **109**, 095302 (2012).
[34] R. A. Williams, M. C. Beeler, L. J. LeBlanc, K. Jiménez-García, and I. B. Spielman, Raman-Induced Interactions in a Single-Component Fermi Gas Near an s-Wave Feshbach Resonance, Phys. Rev. Lett. **111**, 095301 (2013).
[35] D. L. Campbell, R. M. Price, A. Putra, A. Valdés-Curiel, D. Trypogeorgos, and I. B. Spielman, Magnetic phases of spin-1 spin-orbit-coupled Bose gases, Nat. Commun. **7**, 10897 (2016).
[36] X. Luo, L. Wu, J. Chen, Q. Guan, K. Gao, Z.-F. Xu, L. You, and R. Wang, Tunable spin-orbit coupling synthesized with a modulating gradient magnetic field, Sci. Rep. **6**, 18983 (2016).
[37] L. Huang, Z. Meng, P. Wang, P. Peng, S.-L. Zhang, L. Chen, D. Li, Q. Zhou, and J. Zhang, Experimental realization of two-dimensional synthetic spin-orbit coupling in ultracold Fermi gases, Nat. Phys. **12**, 540 (2016).
[38] Z. Wu, L. Zhang, W. Sun, X.-T. Xu, B.-Z. Wang, S.-C. Ji, Y. Deng, S. Chen, X.-J. Liu, and J.-W. Pan, Realization of two-dimensional spin-orbit coupling for Bose-Einstein condensates, Science **354**, 83 (2016).
[39] K. Sun, C. Qu, and C. Zhang, Spin–orbital-angular-momentum coupling in Bose-Einstein condensates, Phys. Rev. A **91**, 063627 (2015).
[40] M. Demarco, and H. Pu, Angular spin-orbit coupling in cold atoms, Phys. Rev. A **91**, 033630 (2015).
[41] C. Qu, K. Sun, and C. Zhang, Quantum phases of Bose-Einstein condensates with synthetic spin-orbital-angular-momentum coupling, Phys. Rev. A **91**, 053630 (2015).
[42] L. Chen, H. Pu, and Y. Zhang, Spin-orbit angular momentum coupling in a spin-1 Bose-Einstein condensate, Phys. Rev. A **93**, 013629 (2016).
[43] L. Jiang, Y. Xu, and C. Zhang, Phase-tunable Josephson junction and spontaneous mass current in a spin-orbit-coupled Fermi superfluid, Phys. Rev. A **94**, 043625 (2016).
[44] J. Hou, X.-W. Luo, K. Sun, and C. Zhang, Adiabatically tuning quantized supercurrents in an annular Bose-Einstein condensate, Phys. Rev. A **96**, 011603(R) (2017).
[45] X.-W. Luo, K. Sun, and C. Zhang, Spin-Tensor–Momentum-Coupled Bose-Einstein Condensates, Phys. Rev. Lett. **119**, 193001 (2017).
[46] H. Hu, F. Zhang, C. Zhang, M. Doublets, and F. Bands, Dirac nodes in s-wave superfluids, arXiv:1710.06388.
[47] T. P. Meyrath, F. Schreck, J. L. Hanssen, C.-S. Chuu, and M. G. Raizen, A high frequency optical trap for atoms using Hermite-Gaussian beams, Opt. Express **13**, 2843 (2005).
[48] C. Reeg, C. Schrade, J. Klinovaja, and D. Loss, DIII topological superconductivity with emergent time-reversal symmetry, Phys. Rev. B **96**, 161407(R) (2017).

[49] C. Chin, R. Grimm, P. Julienne, and E. Tiesinga, Feshbach resonances in ultracold gases, Rev. Mod. Phys. **82**, 1225 (2010).

[50] J.-R. Li, J. Lee, W. Huang, S. Burchesky, B. Shteynas, F. Ç. Top, A. O. Jamison, and W. Ketterle, A stripe phase with supersolid properties in spin-orbit-coupled Bose-Einstein condensates, Nature (London) **543**, 91 (2017).

[51] F. Grusdt, T. Li, I. Bloch, and E. Demler, Tunable spin-orbit coupling for ultracold atoms in two-dimensional optical lattices, Phys. Rev. A **95**, 063617 (2017).

[52] J.-M. Cheng, X.-F. Zhou, Z.-W. Zhou, G.-C. Guo, and M. Gong, Symmetry-enriched Bose-Einstein condensates in a spin-orbit-coupled bilayer system, Phys. Rev. A **97**, 013625 (2018).